The Wing Grid:
A New Approach to Reducing Induced Drag

Final Report
16.622
Fall 2001

David Bennett

Advisor: Eugene Covert **Partner: Todd Oliver**

December 11, 2001

Contents

List of Figures

List of Tables

List of Equations

Abstract

A new design of wing tip, called a wing grid, has been shown to provide a dramatic reduction in the induced drag a wing produces. This experimental project was performed to quantify that reduction and to better understand the wing grid effect. A model wing including three modular wing tips – two different designs of wing grids and a control tip – were constructed and tested at various wind speed and angles of attack in a wind tunnel. The performance of the wing grids relative to the control and to each other was investigated. The experiment showed that at low speeds, the wing grid does not reduce drag, but suggested that it might do so at higher speeds.

1 Introduction

1.1 Background and Motivation

One of the primary obstacles limiting the performance of aircraft is the drag that the aircraft produces. This drag stems from the vortices shed by an aircraft's wings, which cant the local relative wind downward (an effect known as downwash) and generate a component of the local lift force in the direction of the free stream.[1] The strength of this induced drag is proportional to the spacing and radii of these vortices. By designing wings which force the vortices farther apart and at the same time create vortices with larger core radii, one may significantly reduce the amount of drag the aircraft induces. Airplanes which experience less drag require less power and therefore less fuel to fly an arbitrary distance, thus making flight, commercial and otherwise, more efficient and less costly.

One promising drag reduction device is the wing grid, an invention of Dr. Ulrich La Roche of the Fluid Mechanics Laboratory at the Brugg-Windisch School of Engineering in Switzerland. A wing grid provides an innovative method of achieving the vortex arrangement described above. The concept involves constructing wings whose tips are themselves a series of smaller wings, as shown in Figure 1.[2]

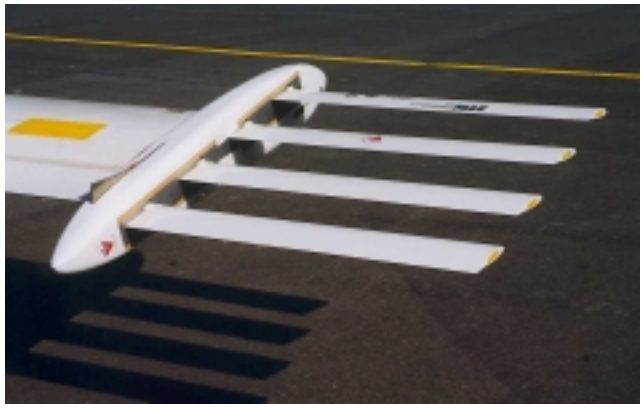

Figure 1: A four-winglet wing grid, used for flight testing in France. The four-winglet configuration has been the subject of this project.

This layout forces the vortices to be shed out along the tips of the winglets, as opposed to being shed along the span of the wing, increasing the vortices' respective radii and moving them farther apart in the span-wise direction (Figure 2). Wings equipped with a wing grid could theoretically experience up to double the lift-to-drag ratio per span of normal wings via rectangular lift distributions.[3] This means that the apparent aspect ratio of a wing with a wing grid is greater than a rectangular wing of the same span, which implies that large wings could be replaced with shorter wings equipped with

wing grids. This structural mass savings augments the fuel mass savings, making the wing grid a great potential asset to flight vehicles.

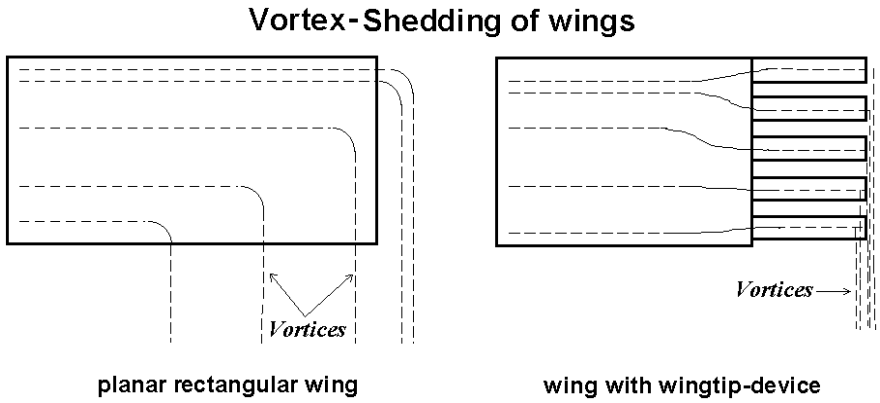

Figure 2: A schematic of the vortex shedding patterns of a normal wing as compared to one outfitted with a wing grid, in which a circulation transfer moves the vortices to the tips of the winglets.[3]

1.2 Objectives

The primary objective of this project was to gather data on subsonic wing grid performance. The degree to which a wing with a wing grid may induce less drag than a comparable wing without a grid was investigated. A secondary objective was to characterize the differences in performance between two wing grid designs, which differ by the loading distribution on the winglets. Force balance data, gathered from wind tunnel tests of wings mounted with wing grids, was used to quantify the wing grids' performance relative to a control rectangular wing and each other.

1.3 Relevant Theory

The velocity of air flow over the top of a cambered wing is greater than that beneath it. This difference in air speed above and below the wing creates a higher pressure below the wing than above, generating lift. However, the higher-pressure air beneath the wing "leaks" around the wingtips, flowing toward the lower pressure zone. This phenomenon leads to the vortices generated in flight, which slightly alter the local free stream air flow and generate downwash, which in turn induces drag. The drag induced by a vehicle in flight is directly related to the kinetic energy of the vortices shed by the wings.[1] This energy is a function of the span-wise spacing of the vortices and their core radius (the Rankine vortex core radius, defined as a solid rotating body, as in Figure 3).

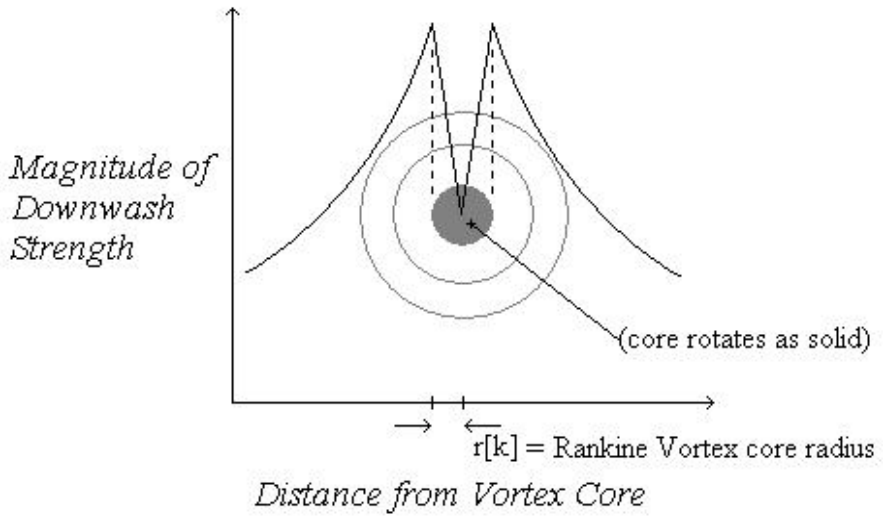

Figure 3: Vortex strength is at a maximum at the outer boundary of the core, and decreases with increasing distance from the center of the core. The vortices carry the same mass flow regardless of core area, implying that those with large radii are weaker than those with small radii.

La Roche defines the function X_{ell} as the ratio of the induced drag of a given wing configuration compared with a plane elliptical wing of the same span. A simplified expression for X_{ell}, the linearized Spreiter and Sacks equation, is given in his reports:

$$X_{ell} = \left(\frac{b}{b'}\right)^2 \left[\frac{1}{16} + \frac{1}{4}\ln\left(\frac{b'-r_k}{r_k}\right)\right] \qquad (1)$$

where b is the given wingspan, b' is the span-wise spacing of the vortices, and r_k is the Rankine Vortex core radius.[3] For a normal rectangular wing, b' and r_k are dependent quantities. This means that if a rectangular wing is designed to increase either b' or r_k, the other decreases, and there is no overall reduction of drag. The wing grid, however, manipulates the air flow over the wing in such a way as to make b' and r_k independent variables. Figure 5 shows that, as both b' and r_k increase, X_{ell} decreases. Therefore, the wing grid's only theoretical limitation in reducing induced drag is the degree to which it can simultaneously increase these two factors.[3] Discussion of the theory underlying the operation of the wing grid is continued in Appendix A.

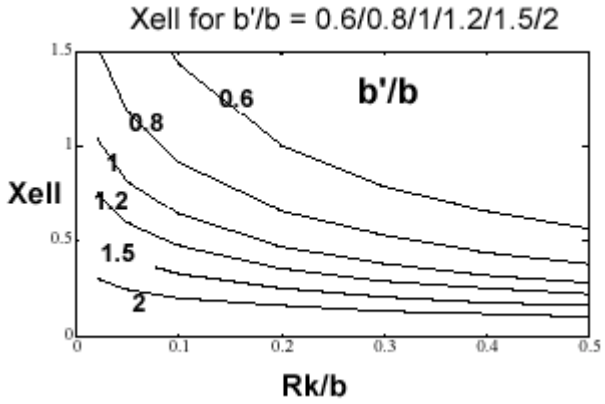

Figure 4: This graph depicts the effect of changing the values of r_k/b and b'/b on the vortex energy generated by a wing.[4]

With this founding theory, it is understood that La Roche's approach to wing design intends to drive b'/b as high as possible while at the same time increasing r_k.[3] This would give shorter-span wings similar lift capabilities to wings with higher aspect ratios.

1.4 Previous Work

Tests were conducted on a model wing with a half aspect ratio (the ratio of the square of the span to the wing area) of 5.[6] at wind speeds up to 145 mph in a smaller wind tunnel than the Wright Brothers Wind Tunnel.

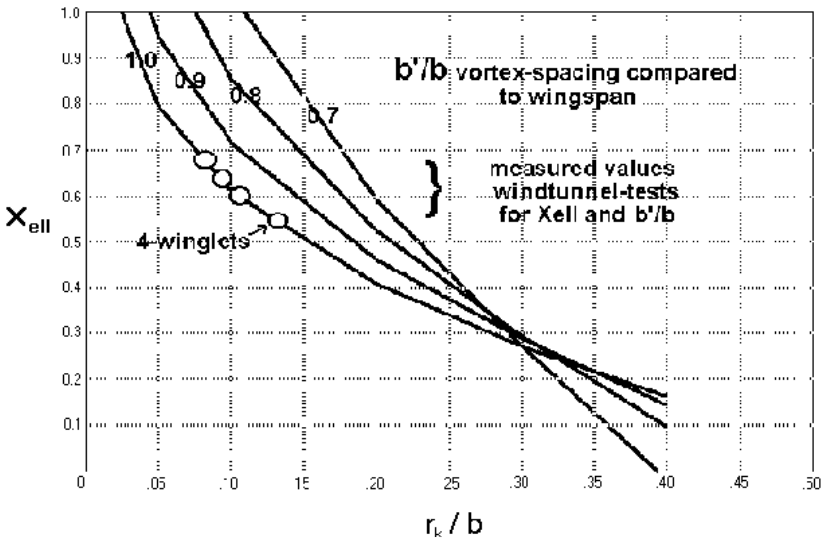

Figure 5: The results of La Roche's wing grid wind tunnel tests are shown above. His results mirror those in Figure 4, showing a 45% reduction in D_i for a four-winglet wing grid.[3]

His successful tests have shown that a wing whose tip (the outer third of the wing model) is replaced by a wing grid with four winglets induces 55% of the drag induced by an planar elliptical wing with the same total span. This point in Figure 5 corresponds to a flow pattern in which the vortex separation is equal to the wing span b and a vortex core radius that is approximately 13% of b. This flow pattern requires a rectangular lift distribution on the wing, a condition difficult to repeat in successive experiments. He notes that below a certain critical speed (or critical Reynolds number), a wing grid behaves like an ordinary slit wing and does not reduce the magnitude of downwash due to massive separation effects.[3] In his tests, La Roche observed this speed to be 45 $^{m}/_{s}$, or 100 mph. Figure 6 plots lift and drag data for multiple wing grids operating below this critical speed. The slope of the curves plotted is a multiple of the wings' span efficiency factor *e*, from[5]:

$$C_{Di} = \frac{C_L^{\,2}}{\pi(AR)e} \qquad (2)$$

where AR is the model's aspect ratio, or the square of its span divided by its planar area. Even for flow regimes in which the wing grid does not reduce drag, the span efficiency of a wing with a wing grid equals or surpasses an elliptical wing of the same span.

It is important to note that, for those experiments La Roche performed which did not produce successful results, the failure was attributed to sub-critical a Reynolds number on the winglets. This meant that the flow over the grid was laminar, allowing it to separate before significant lift was generated.

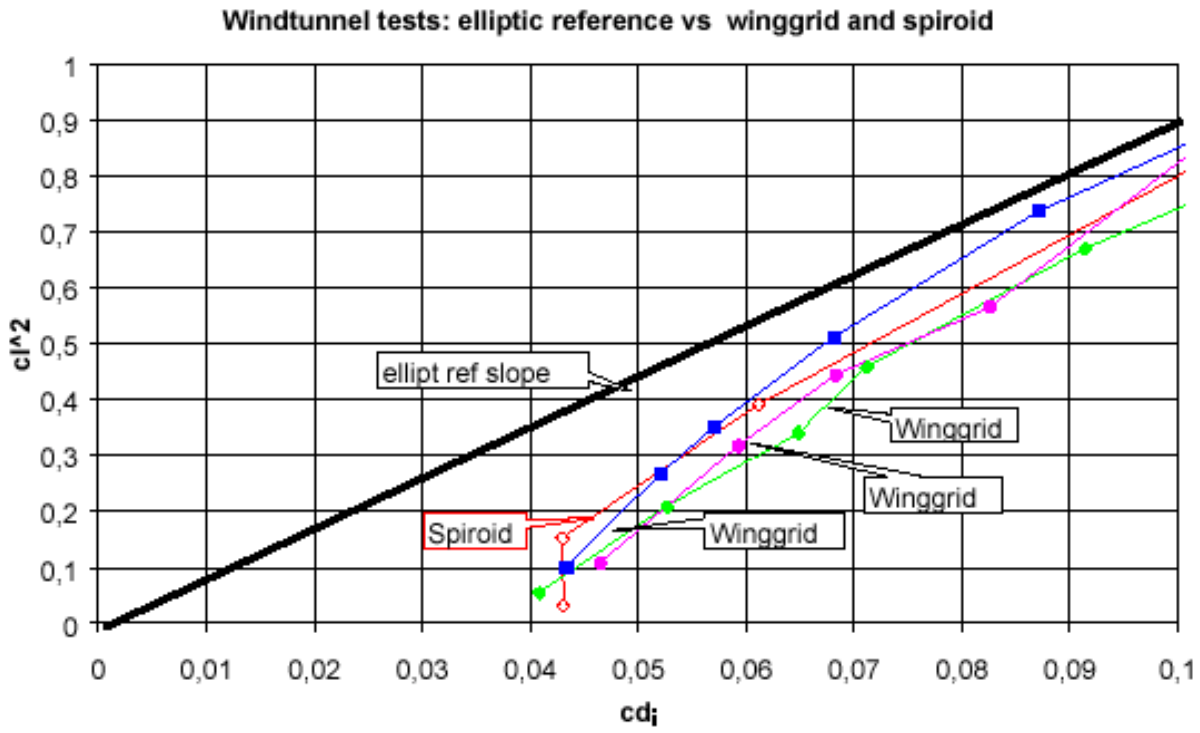

Figure 6: A plot of wing grid performance below the Reynolds number critical for induced drag reduction. This served as a model for lower-speed operation (<100mph).[4]

1.5 Hypotheses

Based on La Roche's experimental results, induced drag reduction of up to 50% could be expected as long as the critical Reynolds number over the wing grid is attained. If the flow over the grid remained laminar, the grid was predicted to behave like a normal slit wing, negatively influencing the ability of the wing with wing grid to generate a rectangular lift distribution. If the wing grid device accomplished induced drag reduction and created the appropriate lift distribution, then wing grid model drag polars were predicted to be above the control, and the model's span efficiency was expected to be greater than 1. If the grids failed to work properly, the opposite results were anticipated.

2 *Technical Approach*

To quantify the extent to which a wing grid reduces the induced drag a wing generates, three wing configurations, each consisting of a main wing body and one of three modular wing tips, were tested in the MIT Wright Brothers Wind Tunnel (WBWT). The wing tips consisted of two different wing grid designs and a control wing tip with the same chord and airfoil type as the main wing. Details of model construction are treated in this section. The completed models were mounted on the six-component pyramidal force balance in the WBWT and moved through a range of angles of attack at three wind speeds. Drag polars were formed from the force data registered on the model at each speed, and plots of C_L^2 vs. C_{Di} were made to compare with La Roche's previous results.

2.1 Model Construction

2.1.1 Wing Grid Design

Two four-winglet wing grids were constructed for this project, one in which all the winglets are at approximately the same angle of attack (AOA) relative to the main wing section, and another in which each winglet experiences roughly the same aerodynamic loading. La Roche provided the empirical methodology to follow in designing the wing grids' geometries. Table 1 summarizes the critical dimensions of each grid.

Table 1: Defining quantities of wing grid geometry.

Grid Type	*Winglet Chord*	*Stagger Angle*	*Winglet Spacing*	*Winglet Rotation Angles*
Equal-AOA	3.1 inches	8.3º	5.2 inches	0º, 0º, 0º, 0º
Equal-Load	3.1 inches	20º	5.1 inches	-13.4º, -8.1º, -4.1º, 1.3º

The stagger angle is defined as the angle between the line of winglets and the chord line of the main wing. Winglet spacing refers to the distance between adjacent winglets' leading edges, and their rotation angles are referenced from the main wing's 0º AOA orientation (listed from leading to trailing winglet). The coordinates defining the winglet airfoil section were also provided by La Roche (see Appendix E). The main wing airfoil was chosen to be the SD7037 because a cusp trailing edge, good low AOA flight characteristics, and a high stall AOA were desirable. The last was important because the wing grids' performance over a large range of AOA was to be investigated.

2.1.2 Superstructure and Wing Sections

The main function of the model's superstructure was to provide the main wing and winglets with appropriate bending stiffness while still being feasible to construct. Thus the main wing section was comprised of two steel spars, one at the quarter-chord and the other at the three-quarter-chord, welded between two steel endplates, as shown in Figure 7.

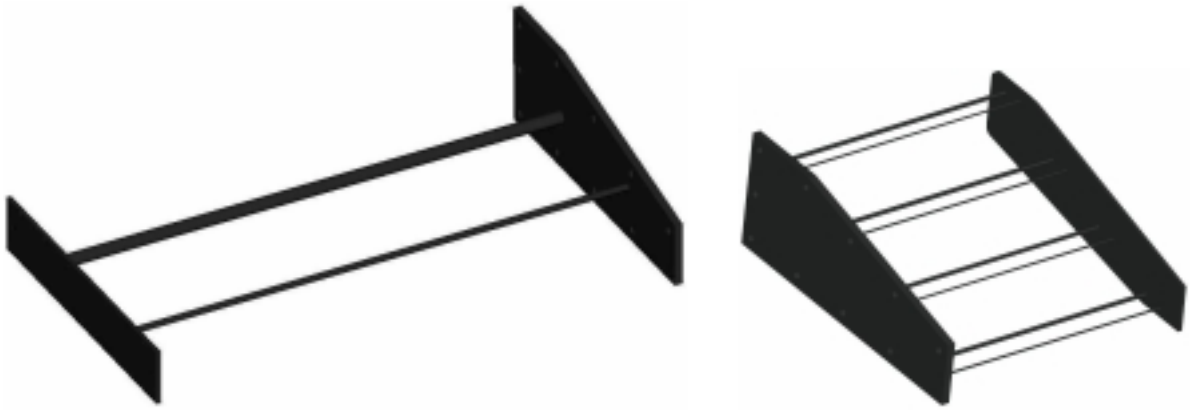

Figure 7: The completed superstructure of the main wing and the Equal-Load wing grid.

The forward spar was thicker, to provide the majority of the required stiffness, while the aft spar served to augment the first and prevent the wing from pitching. The endplates provided a means of attaching the main wing to each of the wing tips and the force balance. The control tip structure was similarly manufactured, as were the wing grids. Each winglet was held in place by fore and aft spars welded between two endplates. The wing and winglets were cut from polystyrene foam using a computer-numerical-controlled hot wire cutter and epoxied to their respective spars. Finally, the wing and winglets were covered in two layers of fiberglass laminate and sanded smooth. The completed models are shown in Figure 8.

Figure 8: From left to right, the finished Equal-Load and Equal-AOA wing grids, and the control tip.

A special piece also had to be created to mate the main wing root endplate to the force balance, which is sunk beneath the tunnel floor. This piece, the force balance interface, is shown in Figure 9. Appendix B contains engineering drawings for all parts of the model.

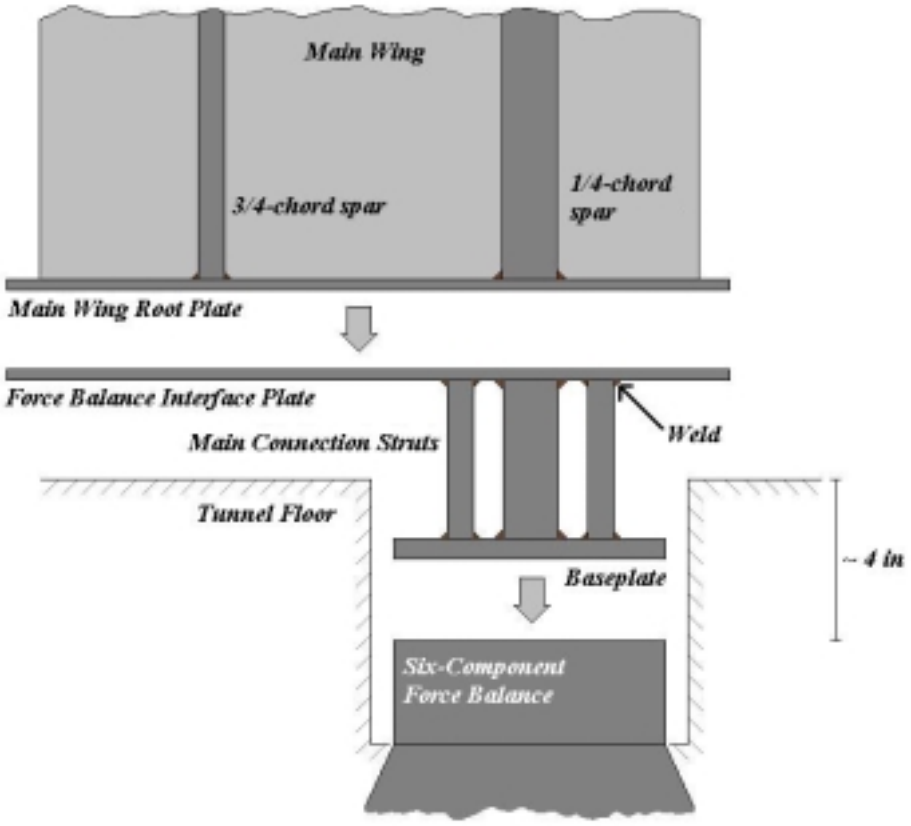

Figure 9: A schematic of the force balance connecting the main wing model to the force balance.

2.1.3 Tunnel Mounting

The model was mounted vertically in the WBWT, as shown in Figure 10. This mounting scheme was chosen for three reasons. First, in this configuration, lift is measured by the force balance as side force, and the balance in the WBWT measures side force most accurately, after drag.[6] Since lift and drag are a crucial quantities in analyzing the experiment's success, the accuracy with which they are measured is important. Second, standing the model in the middle of the tunnel removes it as far as possible from the tunnel walls, thereby minimizing wall effects on the air flow around it. Third, this mounting scheme is easier than using the horizontal mounting apparatus, which would have required building a full-wingspan model. This would have further reduced the size of the wing to fit it in the tunnel, and a smaller wing would have had to have been tested at even higher

velocities to achieve the flow regime (the Reynolds number over the wing grid) in which the wing grid affects the induced drag.

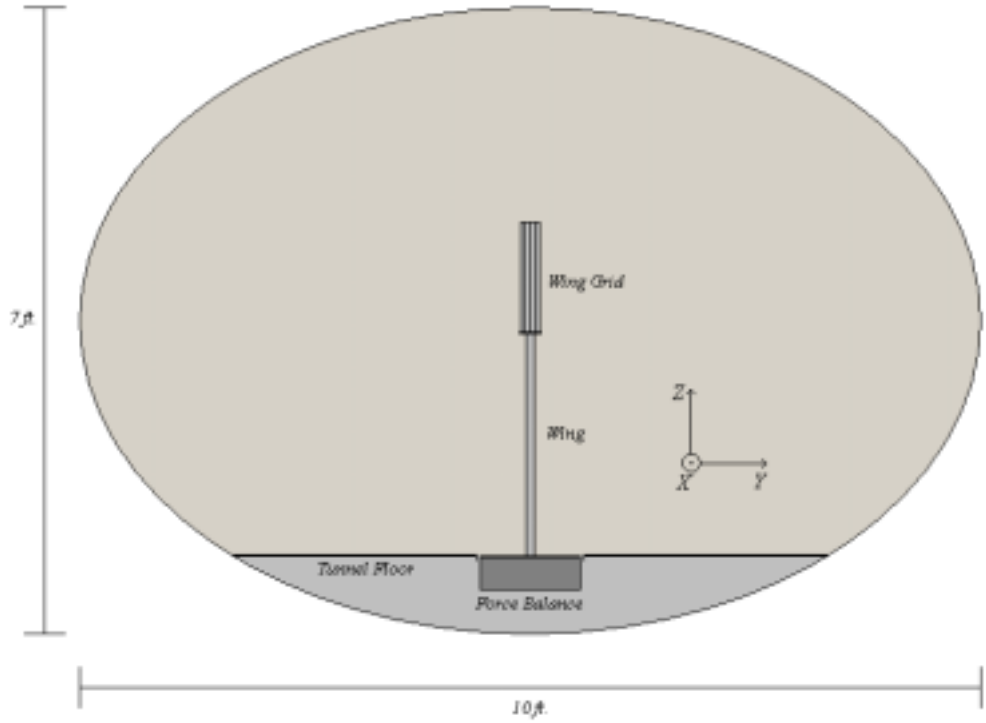

Figure 10: A view from upstream of the wing model mounted in the WBWT.

2.1.4 Weld Failure and Revised Structure

When the control wing configuration was nearing the completion of its testing, the weld attaching the main wing's quarter-chord spar to its root plate failed. The failure occurred when the lift load on the model was 96 lbs (75 mph, 17º AOA). It and the aft spar both broke along the face of the root plate. (See Appendix C for further detail.) This necessitated a new approach to maintaining the model's structural integrity in order to complete testing. Figure 11 illustrates the revised structure. 18-inch stainless steel pipes were fitted with bushings and inserted into the wing to sheathe the main wing spars. Flanges were screwed onto the free ends of the pipes, which protruded from the root of the wing. The flanges were sandwiched between the main wing root plate and the force balance interface to provide more than adequate bending stiffness when the two plates were bolted together. When this entire assembly was completed, three holes were drilled through the main wing, pipe sheathes, and main wing spars. Pins – two at the quarter-chord spar and one at the three-quarter-chord spar – were inserted to hold the spars inside the pipes.

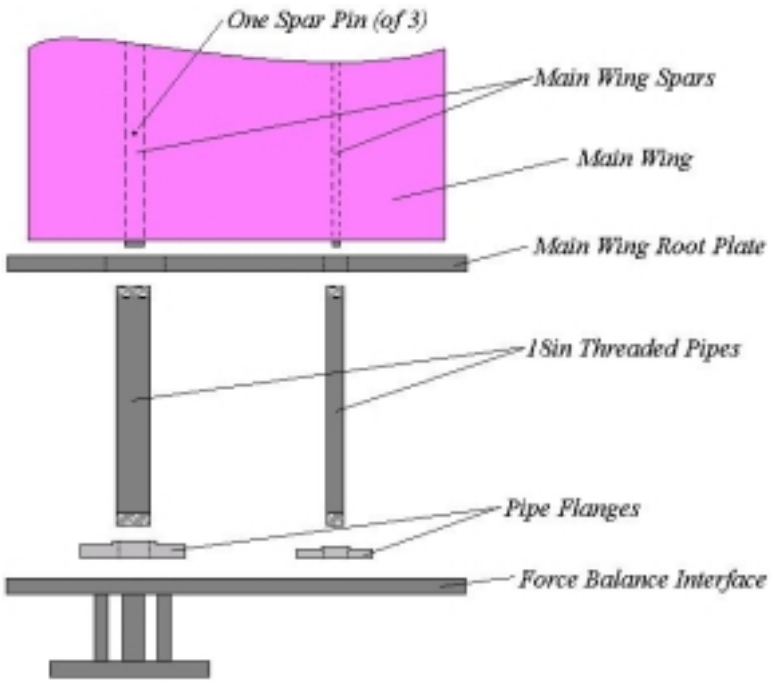

Figure 11: The revised wing root assembly.

2.1.5 Structural Testing

Due to time constraints, the original model was not structurally tested. In redesigning the structure, however, the need for such testing was apparent. The quarter-chord spar pipe was to see the greatest load, and so it was statically tested. The pipe, when screwed into the flange, did not break under 250 ft-lbs of moment and was deemed able to withstand the load it would experience during the remainder of testing. Caution, however, prompted an abbreviated test matrix, as described in section 2.1.6.

2.1.6 Data Acquisition

The wing was angled via the yaw control of the balance to different angles of attack for each flow speed. At each speed, the wing was rotated through angles of attack from 0º to -5º to stall, and back to 0º. After the flow around the wing had settled at each angle of attack, a minute was spent taking data. The readings of lift and drag at each flow condition were averaged into two data points to reduce the influence of noise on the readings. This process was repeated for every angle of attack at a given wind speed, both while increasing and decreasing the wing's inclination, for a total of four averaged readings of lift and drag for each combination of speed and AOA. Table 2 is the project's test matrix.

Table 2: The testing matrix for each of the three wing configurations, showing that four readings were taken at each flow condition.

		-5	-4	…	10	11	…	18
		(° α)						
30	(mph)	4	4	…	4	4	…	4
45		4	4	…	4	4	…	4
60		4	4	…	4	0	…	0

The original test matrix called for running the tunnel at 5 mph increments between 30 mph and 100 mph, in the interests of clearly resolving the speed range over which the wing grid effect occurs. The abbreviated range of flow speeds at which data was taken was a result of the weld failure. As an additional precautionary measure, the safety margin for aerodynamic loading on the model was increased, which accounts for the fact that no data was taken at high AOA at 60 mph. The data output by the wind tunnel data collection software yielded the magnitude of the force components on the wing and a value of dynamic head corrected for humidity, which allowed the lift and drag coefficients to be calculated directly. These coefficients drive the analysis quantifying the wing grids' ability to reduce induced drag.

3 Results

3.1 Data Processing

For each wing configuration at each speed, the drag at zero-lift was determined as well as the data allowed and was subtracted from the measured values of drag to find C_{Di}. From C_L and C_{Di}, drag polars for all the data sets were produced. Polars from the 30 mph data have been omitted because the data was extremely scattered, especially at low AOA, and it was very difficult to establish trends from the plots. Moreover, excluding these data is further justified by the trend visible in the 45 and 60 mph data. The wing grids' performance improved as wind speed increased, so neglecting this data only removes the worst case from consideration.

3.2 Drag Polars

Figure 12 is a plot of the drag polars for all three wing configurations at 45 and 60 mph. It is clear from this graph that neither wing grid outperformed the control wing. Although all three perform similarly at very low AOA, the lift-to-drag ratio of the control quickly surpasses the other two designs.

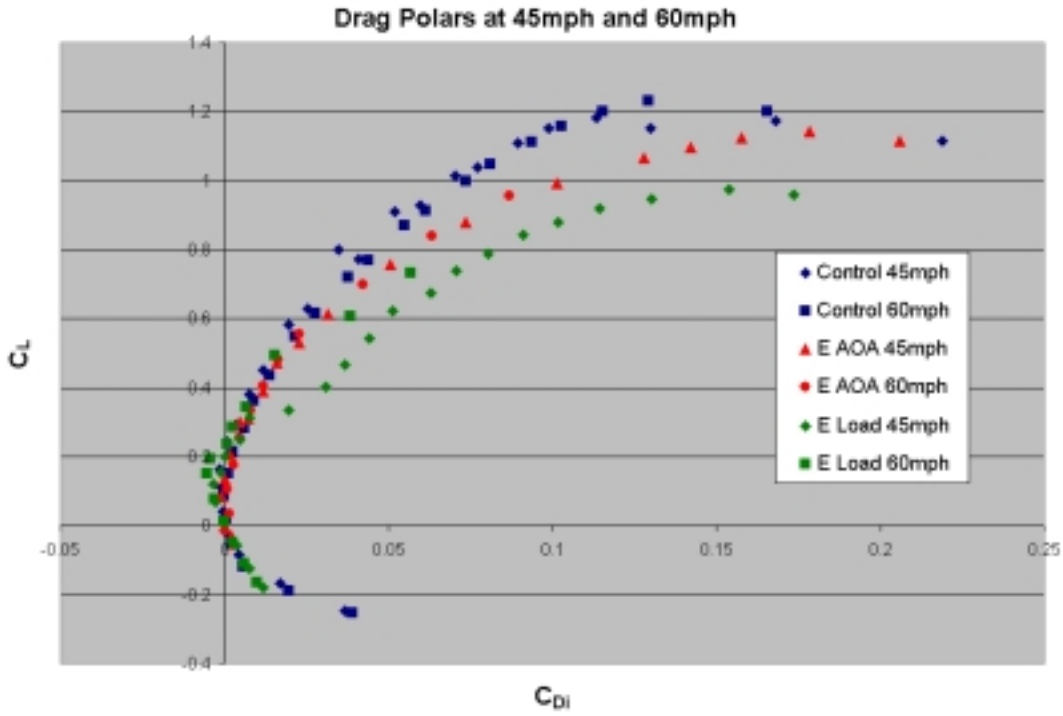

Figure 12: The control wing beat both the Equal-AOA and the Equal-Load wing grid designs in lift-to-drag ratio.

3.3 Span Efficiency Analysis

To gain a deeper understanding of the behavior of the models, plots similar to Figure 6 were made. They show how the span efficiency, a metric of the wing grids' ability to reduce drag on a rectangular wing, changes with AOA at each speed. La Roche's successful wind tunnel tests showed that his half-wing model attained a span efficiency near 2. None of the models in this experiment came close to matching this efficiency, which strongly suggests that the Reynolds number over the wing grids was never large enough to produce a rectangular lift distribution over the wing. Furthermore, the flow separation on the endplates, while unquantified in this analysis, also contributed to the difficulty of maintaining a beneficial lift distribution.

Since the wing model used in this experiment is only a half-wing, care must be taken in calculating *e*, which is in fact the span efficiency of the entire wing. One may imagine that the loading the wing experienced would be symmetrically reflected on the other half of the wing. Therefore, in treating a complete wing, the lift, drag, and span of the model are doubled. This adds a factor to equation 2 which allows *e* to be properly resolved. Equation 3 shows that doubling both lift and span results in the standard equation for the coefficient of lift:

$$2L = \left(\frac{1}{2}\rho V^2\right)(2S)C_L \quad \rightarrow \quad L = \left(\frac{1}{2}\rho V^2\right)SC_L \qquad (3)$$

where the wing area S is the product of wing span b and chord c. The same can be shown in the equation for the coefficient of drag, and the full-span version of equation 2 follows:

$$C_{Di} = \frac{C_L^{\ 2}}{\pi\left(\frac{(2b)^2}{2bc}\right)e} = \frac{C_L^{\ 2}}{\pi(AR_{HW})(2e)} \qquad (4)$$

where AR_{HW} is the aspect ratio of the half wing model mounted in the WBWT. Equation 4 correctly calculates the span efficiency of our wing models from the data collected.

The control wing demonstrated a consistent span efficiency across multiple speeds, as shown in Figure 13. This result was expected and provides validation of the control case.

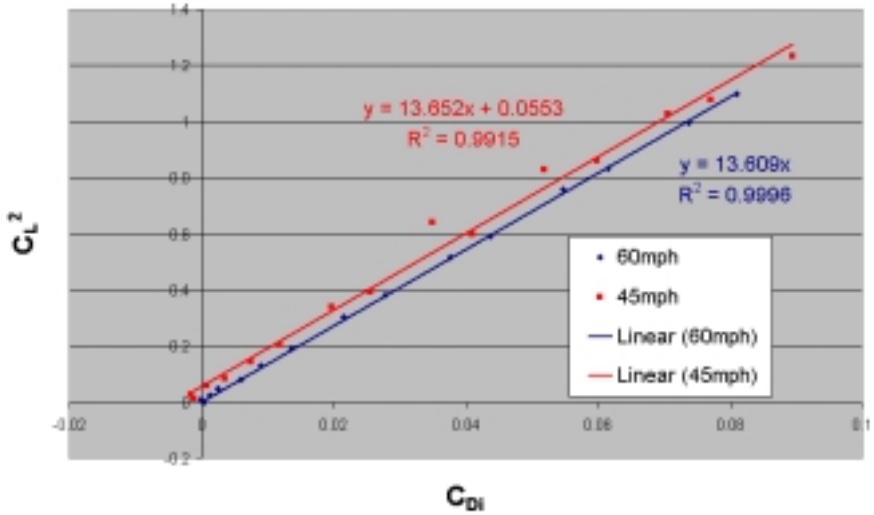

Figure 13: The span efficiency plot for the control wing configuration.

Figure 14 shows the same plot for the Equal-AOA wing grid model at 45 mph. Much like the curves in Figure 6, it appears piecewise linear. The slope of each regression line indicates the approximate span efficiency for that flow regime (low vs. high AOA), as computed from equation 4. Assignment of the range of drag values encompassed by each regime was done visually. At high angles, the wing was half as efficient as at low angles, implying that this wing grid may be better suited to cruise conditions.

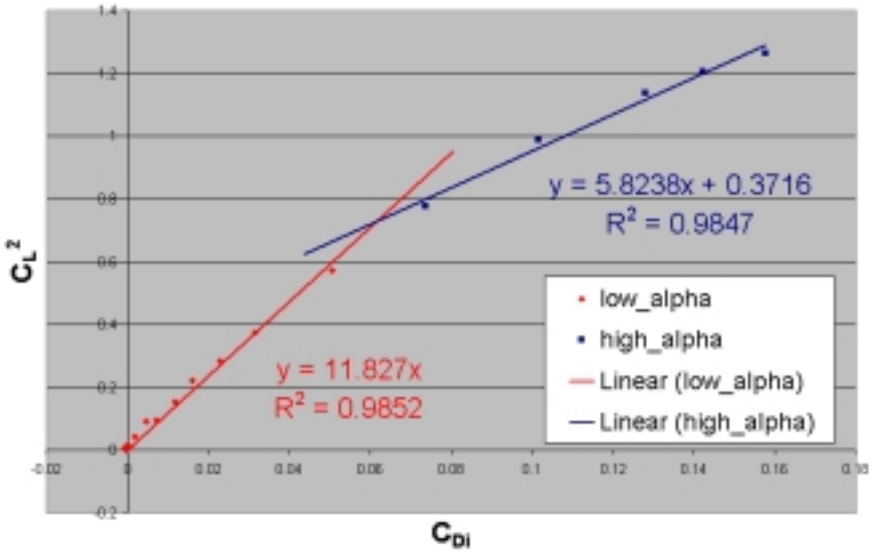

Figure 14: Results from the Equal-AOA wing grid tested at 45 mph.

Figure 15 demonstrated the same trends, although at 60 mph the reduction in span efficiency is lest dramatic. In contrast to the 45 mph case, the transition between the two regions of efficiency occurs at a third of the induced drag at 60 mph. In addition, the low-alpha regime for this case outperformed the control by 2.8%. It should be noted that the range of angles of attack producing this higher efficiency was very limited (-3º to 3º). Still, this data indicates that as wind speed increases, the span efficiency of the Equal-AOA wing grid model improves. It also confirms that this wing grid provides the greatest drag reduction at cruise conditions (low AOA).

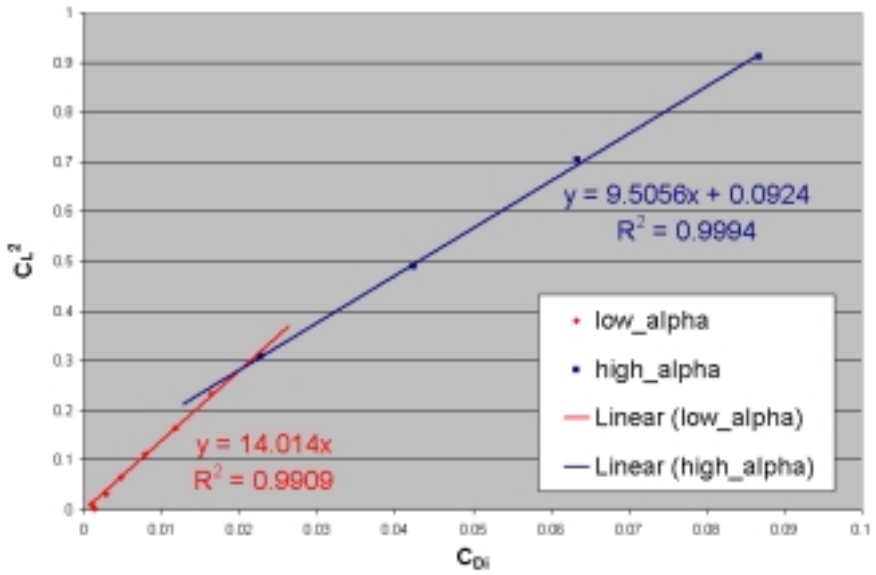

Figure 15: The 60 mph test of the Equal-AOA wing grid.

The Equal-Load wing grid displayed a different behavior from the Equal-AOA grid. When tested at 45 mph, its span efficiency improved for the high-alpha regime rather than deteriorating. This result is shown in Figure 16. In addition, the shift between the two efficiency regions did not occur at a single drag value. Instead, the two regimes were separated by a near-constant lift transition region. The reason for this abrupt increase in drag is as yet unknown, but it could certainly be attributed to a sudden flow separation over the wing grid.

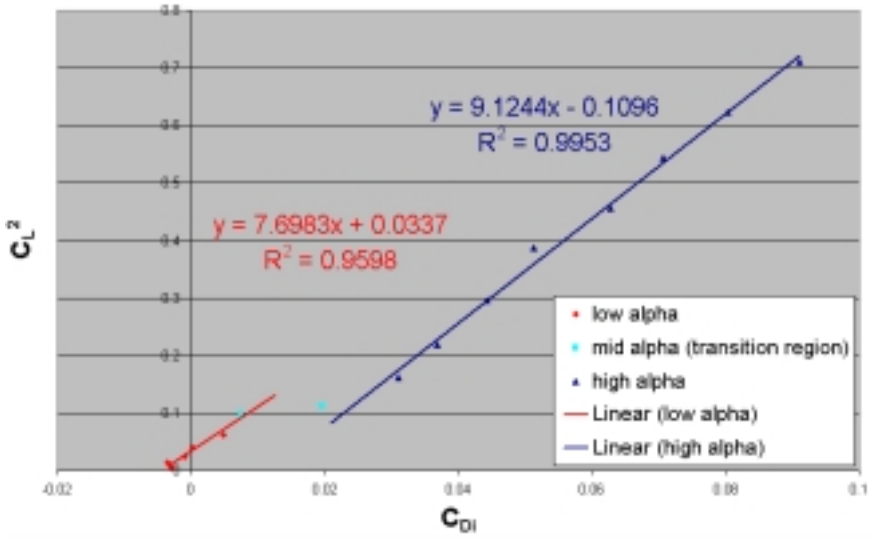

Figure 16: The test results of the Equal-Load wing grid at 45 mph.

The data from the Equal-Load wing grid test at 60 mph was inconclusive. It was determined that an insufficient amount of data had been collected to confidently estimate the ranges of AOA in each efficiency region. The points of negative induced drag were ascribed to error in the force balance's reading of drag. A potential transition region exists, as marked in Figure 17, which makes the data appear to follow the trend of the 45 mph test. More data is required, however, to determine if this assumption is valid.

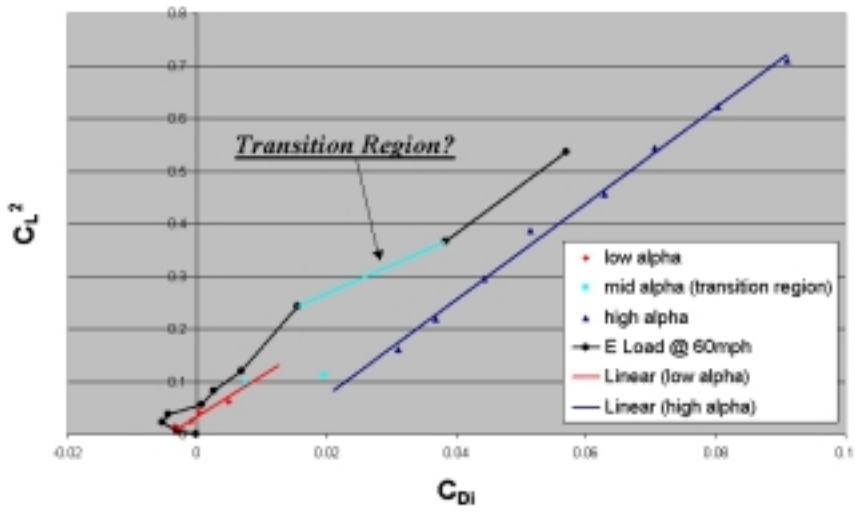

Figure 17: A plot of the Equal-Load data from the 60 mph test superimposed over the span efficiency regions of the Equal-Load wing grid at 45 mph. The data points at 60 mph are connected to illustrate the lift-drag trend, which may indeed reflect that at 45 mph.

Table 3 plots the span efficiencies of each configuration for comparison.

Table 3: Span efficiency calculated from regression lines of each test run.

		Span Efficiency	
Wing Model	V_∞	*Low AOA (Cruising)*	*High AOA (Take-off, Climbing)*
Control	45	.724	.724
	60	.722	.722
Equal-AOA	45	.627	.309
	60	.743	.504
Equal-Load	45	.408	.484
	60	*Insufficient Data to postulate*	

3.4 Discussion of Results

The decreased performance of the Equal-AOA wing grid with increasing AOA is an indication that the flow over the grid separates at the point when the span efficiency drops off. Separation of the flow on the insides of the endplates is also likely to have led to the wing grid's inferior lift generation. The opposite behavior, seen in the tests of the Equal-Load wing grid, is more difficult to explain. The currently existing theoretical models of wing grid behavior at low speeds are insufficient to fully explain this observation. The difference in the span efficiencies of the two AOA ranges is too great to be attributed to error in data collection (described in section 3.5). It is possible that, at higher angles, the flow over the grid became turbulent, thereby allowing the flow to remain attached to the winglets and increasing its lift production. If this were the case, the lift on the wing would have more closely approximated a rectangular distribution, and the span efficiency would have increased, as in Figure G.

3.5 Error Analysis

The error accrued in the measurement of the data was quantified by calculating the standard deviation of the raw data collected from the wind tunnel. With few exceptions, the forces measured in the wind tunnel were consistent with each other to within 5%. Plots of standard deviation of the data are shown in Appendix D. The most widely-varied data was taken at low AOA, when the forces being measured were relatively small. Given that the accuracy of the force balance to measure side force and drag are static quantities – .1 lbs and .03 lbs, respectively – it follows that as the magnitude of the force being measured approaches the order of the error in its measurement, the variance among the measurements will increase.[6]

Non-linear sensitivity analysis revealed the percent change in span efficiency *e* as a function of the percent change in C_L^2 and C_{Di}. Table 4 shows how *e* changes with error in the measurement of C_L and C_D for some extreme cases.

Table 4: The error in calculating *e* from error in determining C_L and C_D.

% Error in…			*% Error in…*	*Relevant Flow Conditions*
C_L	C_D		*e*	
+5	+5	→	+5	High speed, high AOA → high wing loading
-5	-5		-5	
+5	-5		+16	Low speed, low AOA → low wing loading
-5	+5		-14	

When the percent error in C_L and C_D are of opposite signs, the model experienced wobble as it was buffeted by the wind. The wing grids created wakes and eddies that caused the wing to move slightly from side to side. Under these conditions, the accuracy with which span efficiency can be determined decreases significantly, as shown in Appendix D.

4 Conclusions

It is clear from the data gathered that the wing grid has a negative effect on flight performance at low speeds. The flow over it tends to separate before the wing generates a rectangular lift distribution. The critical flow regime, in which the Reynolds number over the grid is sufficiently large and the wing grid effect reduces induced drag, was not reached. The data does, however, imply that at higher speeds, the wing grid effect may be present at low (cruising) angles of attack, as La Roche predicts.

4.1 Future Work

The wing grid is a promising design, and the results obtained in this study demand further work be done to characterize the device's performance over a larger set of flow regimes. All three models – both wing grid configurations and the control – should be tested at speeds at and above 100 mph, so that the critical Reynolds number can be attained. In addition, a functional relationship between span efficiency and flow regime should be determined, or, in lieu of this, a quantified heuristic model. Finally, efforts should be made to connect wing grid theory to a concrete methodology for wing grid design. La Roche's approach is no doubt sound, but still needs to be elucidated for the benefit of the aeronautics community at large.

Acknowledgements

The experimental project team would like to extend warm thanks to the following individuals: Don Weiner for his machine shop expertise and all of his time, Dick Perdichizzi for his invaluable assistance in the wind tunnel, Professor Eugene Covert for his guidance over the past year, and Dr. Ulrich La Roche for his continued correspondence that helped build a better wing grid.

References

[1] Anderson, John D., Jr., "Incompressible Flow over Finite Wings," *Fundamentals of Aerodynamics Second Edition*, 2nd ed., McGraw-Hill, New York, 1991, pp. 316-319.

[2] Ulrich La Roche, Winggrid – The Substitute for Span, http://www.rhone.ch/winggrid/whatisit.htm, last accessed December 08, 2001.

[3] La Roche, Ulrich, "WING-GRID, a Novel Device for Reduction of Induced Drag on Wings," Fluid Mechanics Laboratory HTL Brugg-Windisch, CH-5200, Switzerland, 1996.

[4] La Roche, Ulrich, "Induced Drag Reduction with the WINGGRID Device," Fluid Mechanics Laboratory HTL Brugg-Windisch, CH-8053, Switzerland, 2000.

[5] Anderson, John D., Jr., "Incompressible Flow over Finite Wings," *Fundamentals of Aerodynamics Second Edition*, 2nd ed., McGraw-Hill, New York, 1991, p. 338.

[6] Dept. of Aeronautics and Astronautics, "Characteristics of the Mechanical Balance and Recording System at the Wright Brothers Facility, M.I.T.," 12/9/1987.

Appendices

A Theory

Figure 18 shows the vortex sheets being shed off of winglets and the line vortex on the main wing.

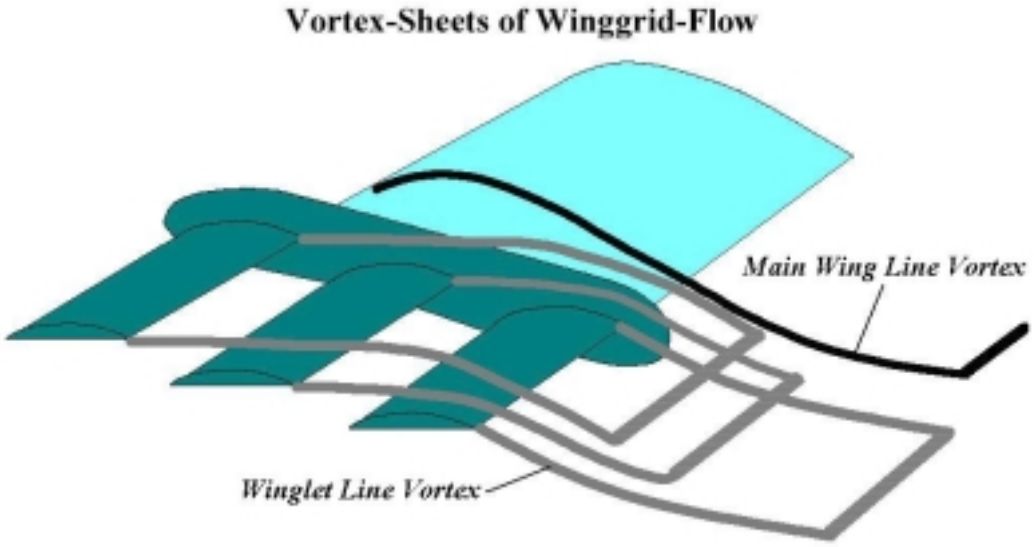

Figure 18: Diagram of the vortices shed by a wing and three winglets.

Each vortex has a cross section which is approximated as a solid core of rotation (the Rankine core), denoted by the gray circle in Figure 3. Outside of the Rankine core radius r_k, the velocity induced by the vortex is inversely proportional to the distance from the vortex. As a result, by moving the vortices farther from the wing, the magnitude of the downwash velocity on the wing decreases, reducing induced drag. The velocity function induced by the vortex line (at r = 0) is given by Equation 5:

$$V(r) = \begin{cases} \frac{r}{r_k} V(r_k), & r<r_k \\ \frac{r_k}{r} V(r_k), & r>r_k \end{cases} \qquad (5)$$

It is true that, for a line vortex, the circulation over the wing can be determined from the line integral of the velocity function, as in Equation 6.

$$\Gamma = \oint V ds = 2\pi r_k{}^2 V(r_k) \qquad (6)$$

For a wing in flight experiencing constant lift, the circulation around it is likewise constant. Therefore, from Equation 6, it is clear that if r_k increases, then $V(r_k)$ must decrease for the circulation to remain constant. Thus, increasing the vortex core radius also decreases the downwash on the wing, leading to reduced induced drag.

B Engineering Drawings

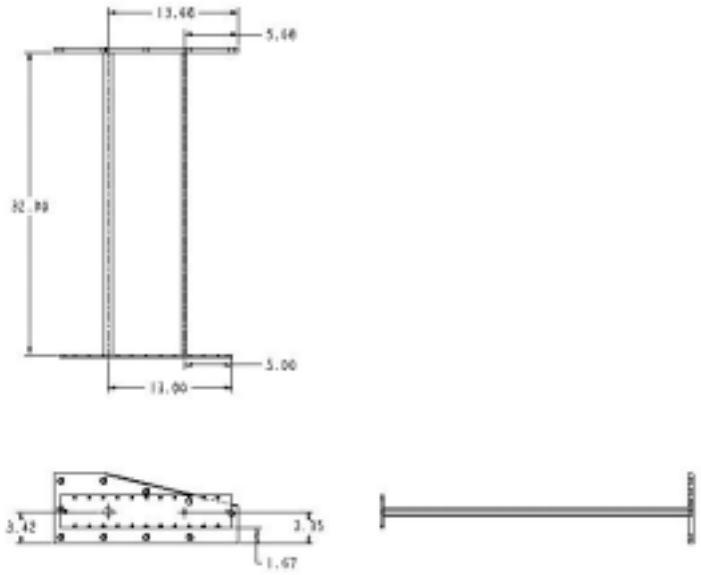

Figure 19: *Main wing structure*

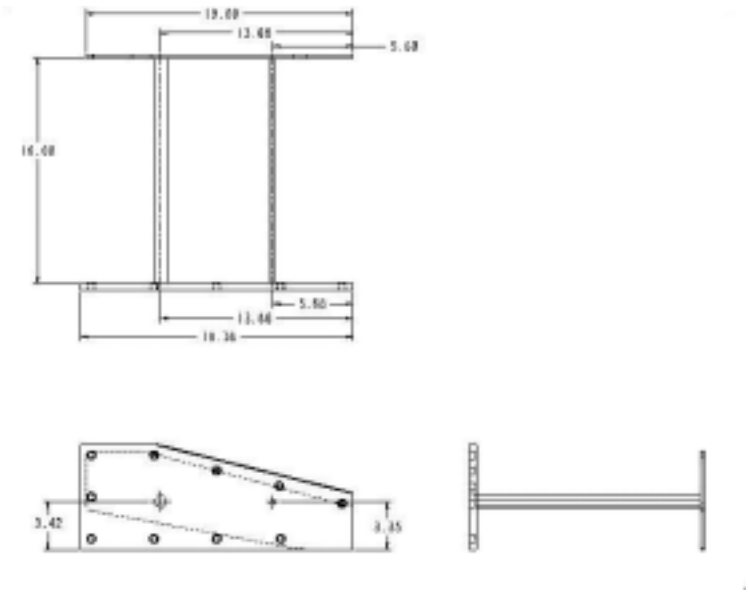

Figure 20: *Control wing tip*

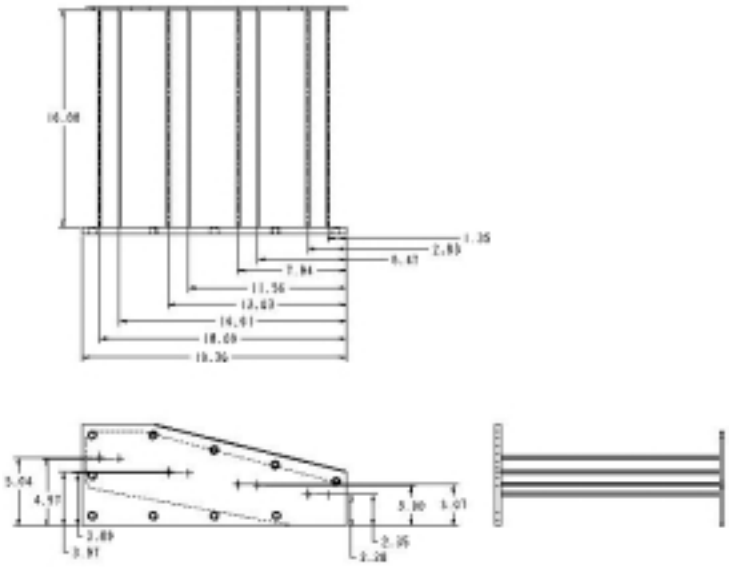

Figure 21: *Equal-AOA wing grid*

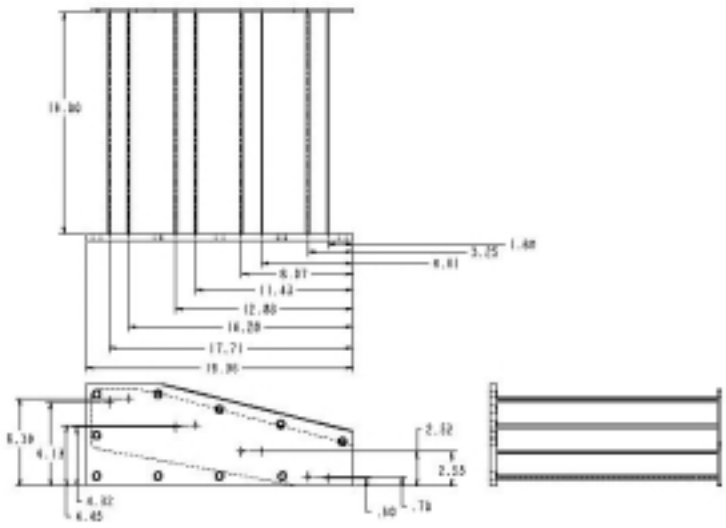

Figure 22: *Equal-Load wing grid*

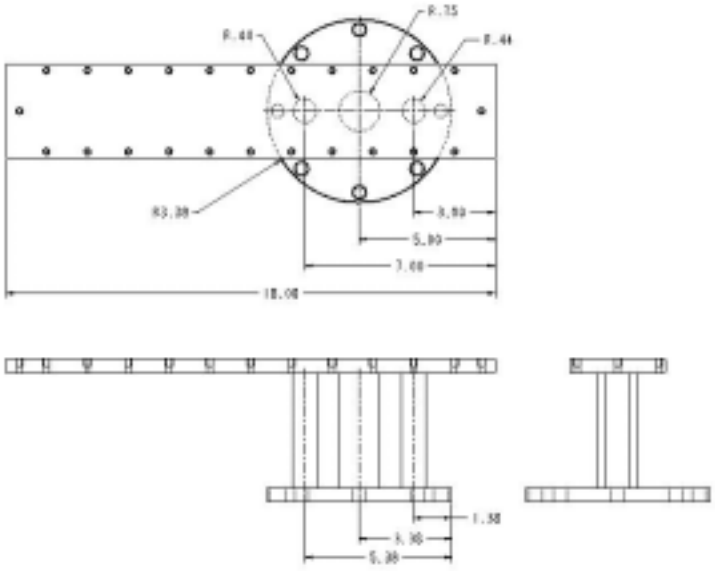

Figure 23: *Force balance interface*

C Weld Failure

The spars for the main wing and winglets were butt-welded into the endplates. That meant drilling clearance holes in the plates where each spar was to be fixed and inserting the spar about half-way into the hole. The spar was then welded inside the hole and the empty space left on the outside of the plate was supposed to be filled in with molten steel and sanded down for a smooth finish. Welding the spar inside of the plate was intended to increase the bending stiffness at the spar/plate interface, essentially making the spars and plates a single piece. Figure 24 schematically shows what was actually done.

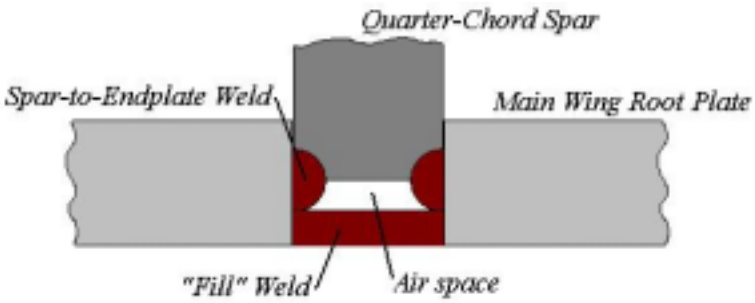

Figure 24: A representation of the way in which the spars were welded to the endplates.

Instead of welding the entire end of the spar and filling the hole completely, the machinist simply welded the circular edge of the spars to the walls of the clearance holes and placed a thin layer of metal over the open end. This severely decreased the amount of bending load the junction could withstand, leading to the failure of the weld under what was thought to be moderate stress. The lessons learned from this incident are two-fold:

1) Always assure that there is adequate communication between the designer and manufacturer. This guarantees that models will be built to specifications.
2) Structural testing may never be neglected, no matter how sturdy a model appears, if its integrity under loading is crucial to the success of the project. In this case, no major damage was done to the WBWT, but was due more to luck than anything else.

D Error Plots

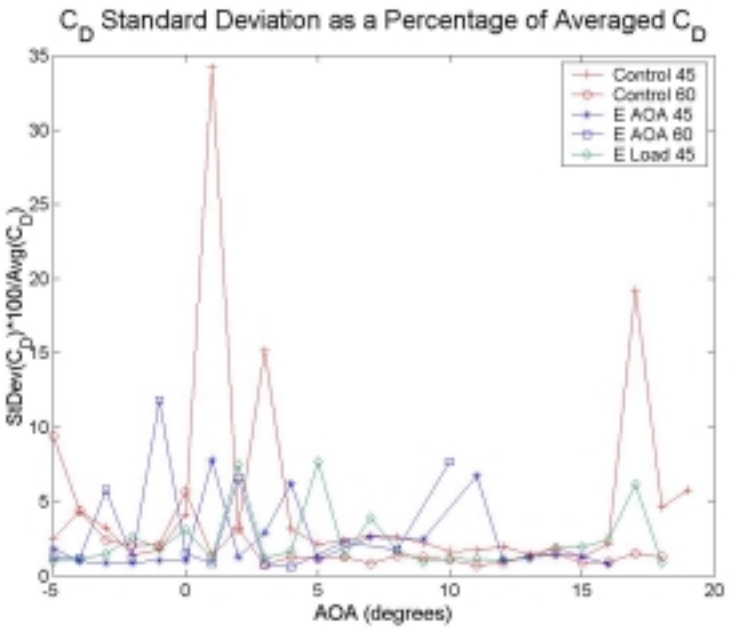

Figure 25: *Standard deviation of raw C_D data*

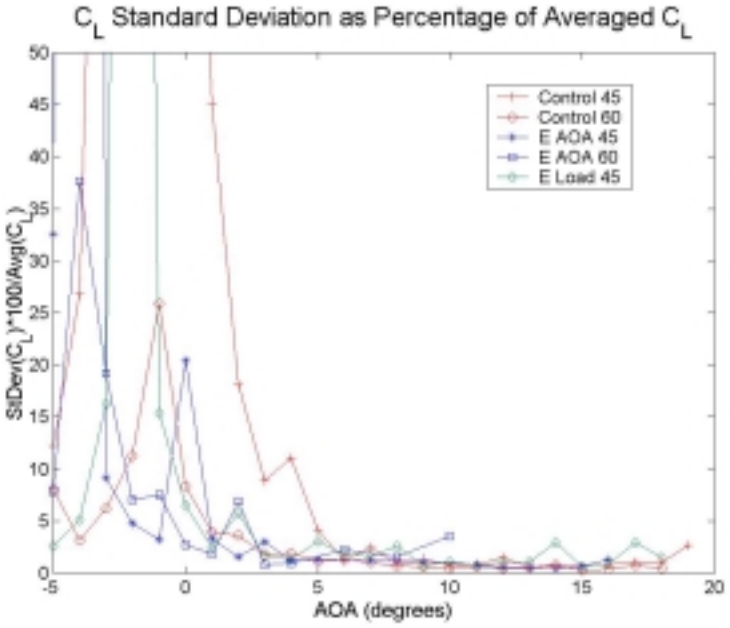

Figure 26: *Standard deviation of raw C_L data*

E Winglet Airfoil

Table 5: *Winglet airfoil coordinates*

X_{TOP}	Y_{TOP}
0	0
0.006156	0.015764
0.024472	0.040687
0.054497	0.067991
0.095491	0.095283
0.146447	0.120157
0.206107	0.140929
0.273005	0.155362
0.345491	0.159802
0.421783	0.151394
0.5	0.133388
0.578217	0.112801
0.654508	0.092726
0.726995	0.074677
0.793893	0.058197
0.853553	0.041956
0.853553	0.041956
0.904508	0.028626
0.945503	0.018659
0.975528	0.009921
0.993844	0.002821
1	0

X_{BOTTOM}	Y_{BOTTOM}
1	0
0.993844	0.000742
0.975528	0.002888
0.945503	0.006192
0.904508	0.010263
0.853553	0.014586
0.793893	0.018573
0.726995	0.021648
0.654508	0.023334
0.578217	0.023357
0.5	0.021718
0.421783	0.018726
0.345491	0.014048
0.273005	0.006235
0.206107	-0.00322
0.146447	-0.01248
0.095491	-0.01971
0.054497	-0.02323
0.024472	-0.02169
0.006156	-0.01413
0	0

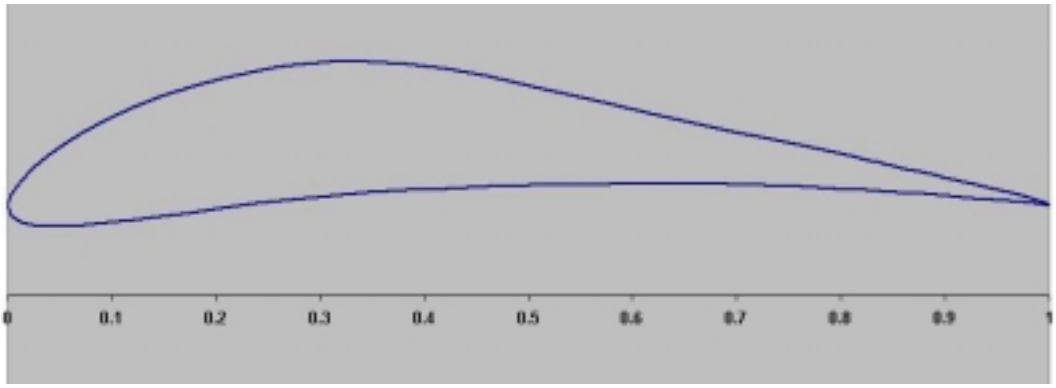

Figure 27: *The winglet airfoil profile*